Ceramics International 44 (2018) 8297–8305

Contents lists available at ScienceDirect

Ceramics International

journal homepage: www.elsevier.com/locate/ceramint

Hydroxyapatite coating containing multi-walled carbon nanotubes on AZ31 magnesium: Mechanical-electrochemical degradation in a physiological environment

Shiva Mohajernia[a,c], Sadegh Pour-Ali[b], Seyedsina Hejazi[a,c,*], Mohsen Saremi[c], Ali-Reza Kiani-Rashid[b]

[a] Department of Materials Science, WW4-LKO, University of Erlangen-Nuremberg, Martensstrasse 7, D-91058 Erlangen, Germany
[b] Materials and Metallurgical Engineering Department, Faculty of Engineering, Ferdowsi University of Mashhad, 91775-1111 Mashhad, Iran
[c] School of Metallurgy and Materials, College of Engineering, University of Tehran, 11155-4563 Tehran, Iran

ARTICLE INFO

Keywords:
AZ31 magnesium alloy
Hydroxyapatite coating
Multi-walled carbon nanotubes (MWCNTs)
Slow strain rate test (SSRT)

ABSTRACT

To control the degradation of magnesium alloys and improve the mechanical performance of common hydroxyapatite (HAp) coatings, a HAp coating containing multi-walled carbon nanotubes (MWCNT) was applied on AZ31 magnesium alloy using plasma spray technique. The coating properties including thickness and morphology, phase analysis and toughness were characterized through SEM, XRD, and indentation methods, respectively. Biodegradation behavior in the presence and absence of slow strain rate test (SSRT) was then thoroughly examined in a simulated body fluid (SBF). The results demonstrated that the stress corrosion cracking (SCC) susceptibility of AZ31 Mg alloy is decreased from 26.8% (HAp coated sample) to 9.8% (HAp/MWCNTs coated one). The combination of microscopic observations as well as mechanical-electrochemical degradation data for long exposure times, suggests that the bridging effect of MWCNTs among molten HAp splats plays a key role in the improvement of mechanical properties and consequently both electrochemical and stress corrosion performances of HAp coating.

1. Introduction

In recent years, biodegradable implant materials have attracted much interest in both medical science and therapeutic engineering [1]. In this way, the biodegradability of different classes of materials including metallic alloys [2], ceramics [3], polymers [4], and composites [5] has been evaluated. Due to relatively high yield strength and fracture toughness, metals have appropriate mechanical properties for biomedical applications [6]; however, this class of materials has two basic problems for such purposes. The first one is that the majority of metals are biologically non-absorbable i.e. further surgeries are needed to remove the implants [7] and the second one is their toxicity which in turn can threaten the human health [8]. The only metal element that does not have mentioned problems is magnesium (Mg).

Mg and its alloys as biodegradable materials are completely comparable with the human bones in density, elastic modulus, and compressive yield strength [9,10]. This element is the fourth most important material in the human body [11]. This fact means that the Mg not only is non-toxic but also it is essential for human metabolism [12]. In spite of these unique advantages, Mg-based implants are of limited use in the clinical applications. The main shortcoming of Mg alloys is their low corrosion resistance in chloride containing solutions including physiological environment (pH = 7.4–7.6) [13]. High concentrations of Mg (serum levels more than 1.05 mmol/L) as a result of enhanced corrosion can lead to muscular paralysis, hypotension, respiratory distress and even cardiac arrest [10,14]. In addition, Mg corrosion in the body is involved a lot of gas bubbles and local pH increase which are disturbing for bone tissue healing [15].

In the past decade, various approaches have been investigated to improve the corrosion behavior of Mg in the physiological environments. Among them, surface engineering and coating application have been documented as the most effective methods [16–18]. Using modified hydroxyapatite (HAp) coatings is one of the most recent and hopeful methods to overcome the mentioned problem (low corrosion resistance of Mg alloys) [19–21]. Among different modified HAp coatings, plasma-sprayed multi-walled carbon nanotubes (MWCNTs) reinforced HAp coatings have greater mechanical properties (especially fracture toughness). Based on a report by Balani et al. [22], plasma

* Corresponding author at: Department of Materials Science, WW4-LKO, University of Erlangen-Nuremberg, Martensstrasse 7, D-91058 Erlangen, Germany.
E-mail address: sina.hejazi@fau.de (S. Hejazi).

https://doi.org/10.1016/j.ceramint.2018.02.015
Received 1 January 2018; Received in revised form 26 January 2018; Accepted 2 February 2018
Available online 03 February 2018

spraying of HAp–4 wt% MWCNT powder on titanium alloys led to a uniform distribution of undamaged CNTs, high adhesion strength, improvement in the fracture toughness by 56%, and an increase in the crystallinity from 53.7% to 80.4%. Similarly, there are other studies which have been inclined to modify the mechanical properties of HAp coatings through MWCNTs [23–25]; however, two important issues should be well thought out from previous works. The first one is that these efforts have been focused on the substrates other than Mg alloys and it is necessary to fix this deficiency and the second one is the consideration of synergistic presence of the mechanical loading along with the corrosive environment on implant material which may lead to a more complicated premature failure of implants (i.e. due to the phenomenon of stress corrosion cracking (SCC), fracture can occur even at stresses considerably lower than the yield and design stresses [26]). In the present work, we tried to consider both mentioned problems. In this way, HAp powder containing MWCNTs was sputtered on AZ31 Mg alloy by plasma spray method. Different analyses methods including scanning electron microscopy (SEM), X-ray diffraction (XRD) and indentation measurement were employed to characterize the synthesized coating. In addition, the electrochemical corrosion and SCC performances of the coated alloy were evaluated by potentiodynamic polarization, electrochemical impedance spectroscopy (EIS), and slow strain rate tensile (SSRT) coupled with electrochemical noise (EN) tests in a simulated body fluid (SBF).

2. Experimental procedure

2.1. Materials and processing

AZ31 Mg alloy was used as the substrate with chemical composition as follows (wt%): 3.05 Al, 0.82 Zn, 0.40 Mn, 0.02 Si, 0.003 Cu, 0.001 Ni, 0.002 Fe and Mg balance. Prior to the coating application, AZ31 Mg samples were ground with SiC abrasive paper (up to 2000 grit), polished with diamond paste (particle size 3 μm), and then ultrasonically cleaned in ethanol for 10 min and dried at room temperature. Commercial hydroxyapatite powders (HAp, SAI, France, particle size: 65–85 μm) and MWCNTs (Jiangsu, purity: 99% +, diameter: 10–20 nm, length less than 1 μm) were used as precursor materials for the spray feedstock (MWCNTs have a Young's Modulus of approximately 1–2 TPa, tensile strengths in the range of 30–180 GPa, and a specific surface area of up to 150 m^2/g). A combination of HAp powder and MWCNTs corresponding to HAp–4 wt% MWCNTs was mechanically milled for 18 h to obtain a homogeneous mixture [22,27]. In order to improve the mill efficiency, Nylon ball-milling pot with Agate balls (diameter 0.5–2.0 cm) was used. The powder to ball weight ratio of 1:5 was kept constant during the milling process. Ball milling parameters have been shown in Table 1. Plasma spraying of HAp powder and HAp/MWCNTs mixture was carried out using A3000s Plasma Technik–F4 gun with optimized spray parameters presented in Table 2. Powder feedstocks were injected with Ar carrier gas to result in the coatings onto AZ31 Mg substrates.

2.2. Microstructural and mechanical characterization

SEM microscopy (Oxford S360, Cambridge, UK, JEOL JSM-6310) was used for microstructural analysis. X-ray diffraction spectrum was obtained using Philips Xpert MPD at 40 kV and 20 mA with Cu-K_α peak. The fraction of crystalline HAp phase (%*C*) present in the coatings was calculated using Eq. (1):

$$\%C = \frac{\sum A_{\mathrm{HAp}}}{\sum A_{\mathrm{all-peaks}}} \quad (1)$$

Where A_{HAp} is the area under the HAp peaks and $A_{\mathrm{all\_peaks}}$ is the area under all peaks. HXD-100 TMC Lenovo Vickers microhardness tester was also used for estimating the fracture toughness of the HAp and HAp/MWCNTs coatings. Indentation toughness of the coatings was calculated for a load of 100 g and dwell time of 15 s using Eq. (2) [22]:

$$K_{\mathrm{IC}} = 0.016\left(\frac{E}{H}\right)^{0.5} P{\cdot}c^{-1.5} \quad (2)$$

Where K_{IC} is the fracture toughness of coating (MPa.$m^{0.5}$), *E* is Young's modulus (GPa), *H* is the hardness (GPa), *P* is the applied force (kgf) and *c* is the average crack length (mm) from the center of indent.

2.3. Electrochemical corrosion measurements

Potentiodynamic polarization and electrochemical impedance measurements (EIS) were carried out in an electrochemical system (An EG & G potentiostat 273A along with a Solarton frequency response analyzer SI 1255 for EIS measurements) with a conventional three-electrode cell of saturated calomel electrode (SCE) as the reference electrode, a platinum counter electrode, and a sample with 1 cm^2 area as the working electrode. All electrochemical experiments were run after 60 min to reach the open circuit potential (OCP) and afterwards conducted with the SBF as the electrolyte at 37.0 ± 0.5 °C. The chemical composition of the SBF has been presented in Table 3. To get rid of gas bubbles that may appear on the surface of corroding samples, the electrolyte was de-aerated by bubbling nitrogen for 30 min. Potentiodynamic polarization tests were carried out in the range of ± 250 mV respect to the OCP with a scan rate of 0.2 mV/s. The impedance measurements were performed in the frequency range of 100 kHz to 10 mHz using an AC overpotential with an amplitude of 5 mV around OCP.

2.4. SCC and EN measurements

SCC susceptibility of different samples was evaluated at 37.0 ± 0.5 °C using SSRT testing in SBF and free air. By using a DC control motor with reduction gear box, dog-bone shaped samples with gauge dimensions of 30 mm (length), 6 mm (width) and 2 mm (thickness) were pulled with a 1.2×10^{-7} /s strain rate until fracture. After this test, the fracture surfaces were cleaned with chromic acid and then examined using SEM. While carrying out the SSRT tests, EN test in a freely corroding system was also performed with a setup similar to the

Table 1
The parameters selected for ball milling process.

	Ethanol (mL)	MWCNTs (g)	HAp (g)	Time (h)
HAp/MWCNTs	50	2.0	48.0	18
HAp	50	0	50.0	18

Table 2
The spray parameters for the depositing of HAp and HAp/MWCNTs coatings.

Ar (L/min)	N_2 (L/min)	Current (A)	Powder feed rate (g/min)	Powder gas Ar (L/min)	Spray distance (cm)
25	2	400	30	4	8

Table 3
The chemical composition of SBF.

Reagent	Amount
NaCl	8.035 g
KCl	0.225 g
$NaHCO_3$	0.355 g
$MgCl_2{\cdot}6H_2O$	0.311 g
$K_2HPO_4{\cdot}3H_2O$	0.231 g
HCl (1.0 M)	39.0 mL
$CaCl_2$	0.292 g
Na_2SO_4	0.072 g
Tris buffer	6.110 g

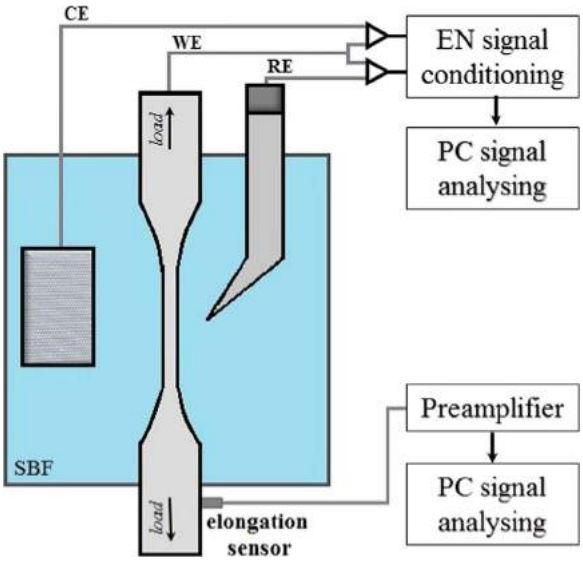

Fig. 1. Schematic of the SSRT experimental set-up.

other electrochemical measurements (Fig. 1). A NI cFP–Al–118 module was applied to acquire the potential and current data. The potential and current were amplified and digitized by using a 16–bit A/D converter with a resolution of 0.03 mV and 0.3 nA. It is worthy to note that the noise data were transformed into the frequency domain using fast Fourier transform (FFT) algorithm and fast wavelet transform algorithm (FWT). For the FFT, power spectral density (PSD) was calculated in a frequency domain from 10^{-3} to 0.5 Hz.

3. Results and discussion

3.1. Coating characterization

Figs. 2a and b show SEM images from the cross section of HAp and HAp/MWCNTs coatings. It is evident from these images that the coatings bonded to the substrate through fusion bonding. In both cases, the fine pores are uniformly distributed throughout the coating. These pores are in the nature of plasma spray coatings. The results of Microstructure Image Processing (MIP) software displayed porosity content less than 10% for the both coatings. As reported by Chen et al. [23], these pores which have little interlinking are very helpful for mechanical fixation of living bone tissues. The coatings are almost uniform in the thickness and appear microstructurally homogeneous. The average thickness of HAp and HAp/MWCNTs coatings are 122.2 ± 6.9 μm and 125.6 ± 9.1 μm, respectively. The surface morphology of HAp and HAp/MWCNTs coatings in different magnifications are presented in Figs. 2c-f. As can be seen from these images, the surface microstructure has been mainly consisted of well-flattened/accumulated splats (fully molten, as shown by arrowhead 1) and spheroidized particles (semi molten and non-molten particles, as shown by arrowhead 2). These microstructural features lead to a rough surface for the both coatings. In contrast to the HAp coating, HAp/MWCNTs one

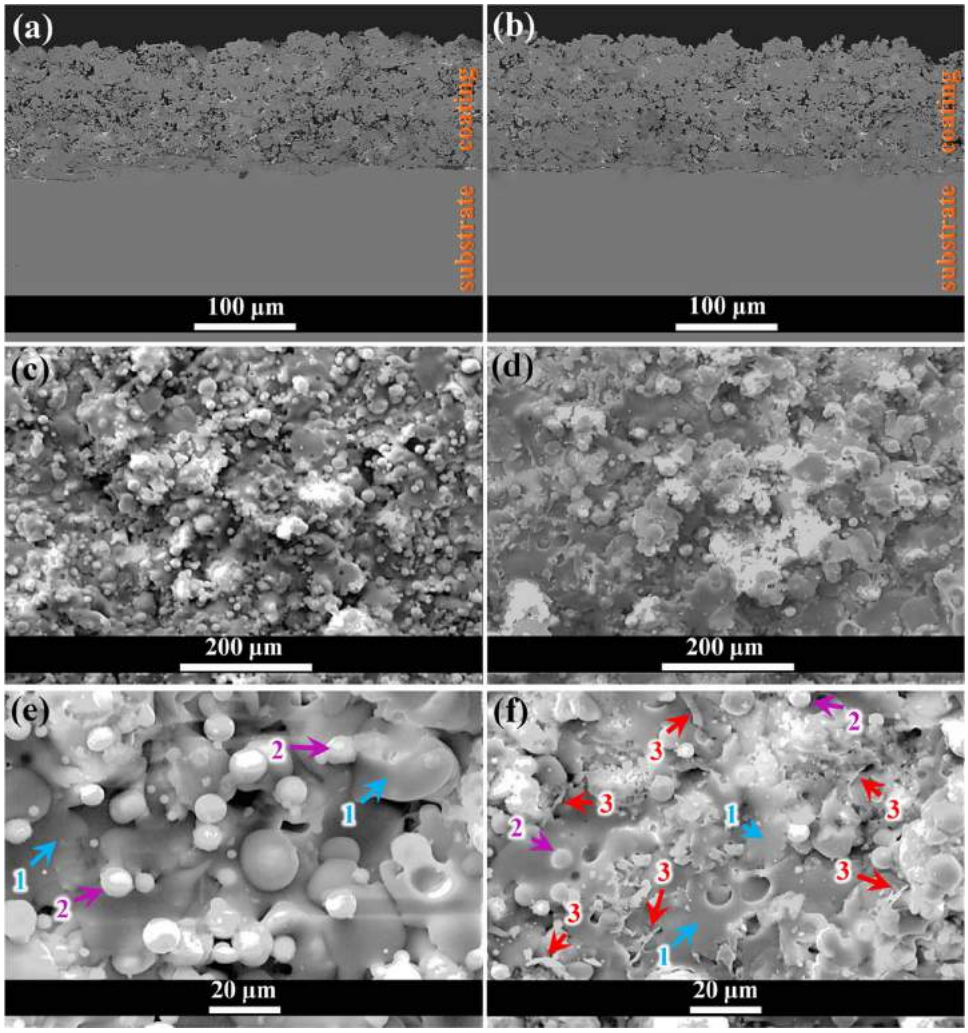

Fig. 2. SEM images taken from the cross-section of (a) HAp and (b) HAp/MWCNTs coatings and the surface of as-sprayed (c and e) HAp and (d and f) HAp/MWCNTs coatings.

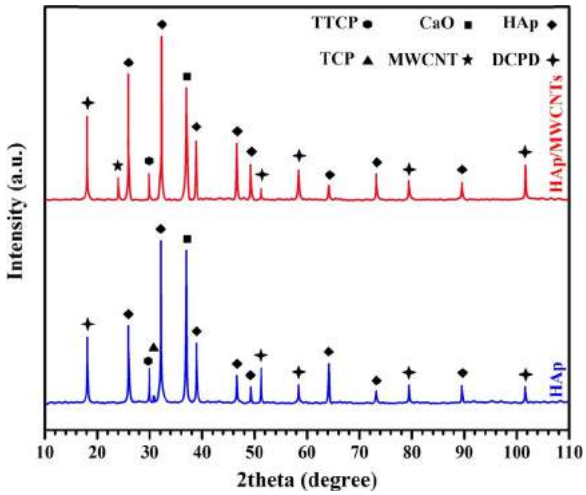

Fig. 3. XRD patterns of the HAp and HAp/MWCNTs coatings.

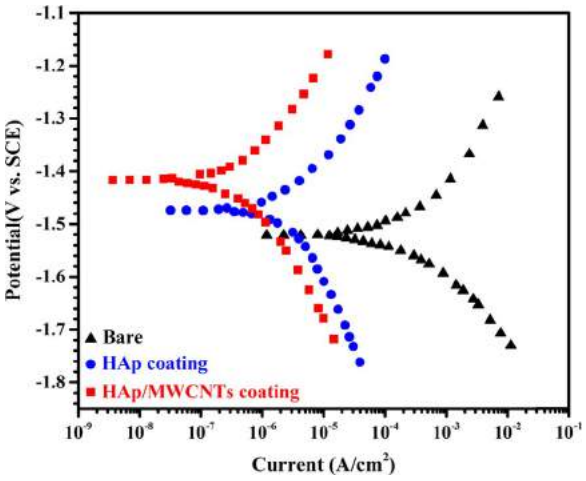

Fig. 5. Potentiodynamic polarization tests of different samples in SBF.

shows a unique microstructural characteristic and that is the MWCNT-bridging at the splat-splat interfaces (see Fig. 2f, arrowhead 3). As a result of the high melting point of MWCNTs, they can remain intact during plasma spraying and act as bridges between melted and/or semi-melted splats. It is notable that in Fig. 2f, the widths of bridges are several times bigger than the diameter of MWCNTs. This can be attributed to the precipitation of HAp splats over the MWCNTs surface during plasma spraying. This phenomenon increases the reinforcing effect of MWCNTs [22,28].

The phase composition of the plasma sprayed coatings was characterized by XRD analysis. As shown in Fig. 3, the constituent phases of the coatings are HAp, CaO and dicalcium phosphate dihydrate (DCPD) with some low intensity peaks related to tetracalcium phosphate (TTCP), MWCNTs (only for HAp/MWCNTs coating) and tricalcium phosphate (TCP, only for HAp coating). The presence of MWCNTs peak and absence of any carbide peaks in the XRD pattern of HAp/MWCNTs coating indicating that the MWCNTs in the precursor materials have not been reacted with the substrate and HAp powder during coating application. It is worthy to note that the small fraction of other possible phases is difficult to detect within the sensitivity limit of XRD. HAp coating represented crystallinity of 55.4% whereas HAp/MWCNTs coating has a crystallinity of 71.1% which shows that the amount of secondary phases (CaO, TCP, TTCP and etc.) has been decreased in the presence of MWCNTs. Achieving a higher degree of crystallinity, by itself, can improve the mechanical and biocompatibility properties of the HAp coating [29].

Fig. 4 shows the results of Vicker's indentation toughness for the both coatings. As can be seen, the fracture toughness of HAp/MWCNTs

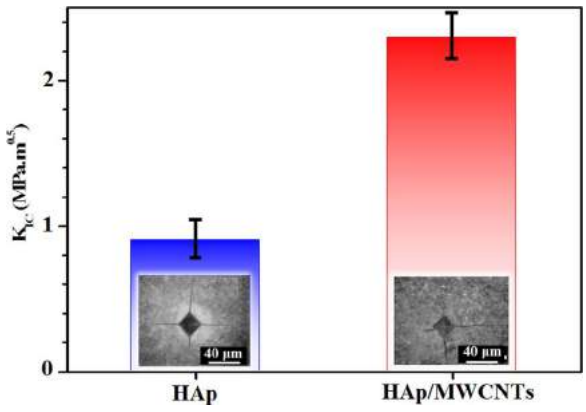

Fig. 4. The fracture toughness of HAp and HAp/MWCNTs coatings (indentation impressions have been shown as inset).

coating is considerably higher than HAp one (2.13 ± 0.29 MPa/m$^{0.5}$ compared to 0.91 ± 0.16 MPa/m$^{0.5}$). This increment in the fracture toughness can be attributed to two main reasons. Firstly, MWCNTs can act as bridges (see Fig. 2f) and restrict the widening of the cracks. In fact, MWCNTs bridges require more energy for opening up of the cracks and cause toughening [30]. Secondly, a lower amount of secondary phases (higher degree of crystallinity) is also improved the mechanical properties of the HAp coatings especially their fracture toughness [22].

3.2. Electrochemical evaluation

Fig. 5 shows the polarization curves of different samples in SBF at 37.0 ± 0.5 °C. Electrochemical parameters derived from these plots including corrosion potential (E_{corr}), corrosion current density (i_{corr}) and cathodic (b_c) and anodic Tafel slopes (b_a), which were measured using Tafel extrapolation of the anodic and cathodic lines, are listed in Table 4. As can be seen from Fig. 5, the overall shape of polarization curve is not changed in the presence of both coatings, so it can be claimed that these coatings don't affect the corrosion mechanism of AZ31 Mg alloy. As can be assessed from Fig. 5 and Table 4, corrosion performance of AZ31 Mg alloy is improved in the presence of HAp and HAp/MWCNTs coatings. The E_{corr} of the AZ31 Mg alloy increased from −1.521 V vs. SCE to –1.465 and −1.417 V vs. SCE for HAp and HAp/MWCNTs coatings, respectively. This shifting towards more noble values implying a decrease in the tendency of corrosion initiation due to the thermodynamics. In addition, the i_{corr} of HAp/MWCNTs coated sample (3.7×10^{-7} A/cm^2) is approximately one order of magnitude (4.1×10^{-6} A/cm^2) and three orders of magnitude (3.5×10^{-4} A/cm^2) lower than HAp coated sample and bare one, respectively. These results clearly demonstrate that the HAp/MWCNTs composite coating provides a great protection from corrosion attack.

Impedance technique is known as one of the most powerful methods to evaluate the durability of coatings [31]. Thus, EIS was performed in order to obtain additional insight into the corrosion of AZ31 Mg alloy protected by HAp and HAp/MWCNTs coatings in SBF at various immersion times up to 30 h. For instance, Fig. 9 represents the Nyquist and Bode modulus plots of different samples in the test solutions after two different exposure times (60 min and 30 h). In the case of the bare sample, a capacitive loop in the high and medium frequency ranges and an inductive loop in the low frequency ranges are observed in the Nyquist plots (Figs. 6a and b). As it has been widely reported [32,33], the capacitive loop is related to the charge transfer process, whereas the inductive loop can be attributed to the dissolution of AZ31 Mg alloy. Moreover, the bigger capacitive loop and larger low-frequency impedance modulus indicate a better corrosion protection performance [32–34]. So, the decrease in the diameter of the capacitive loop and

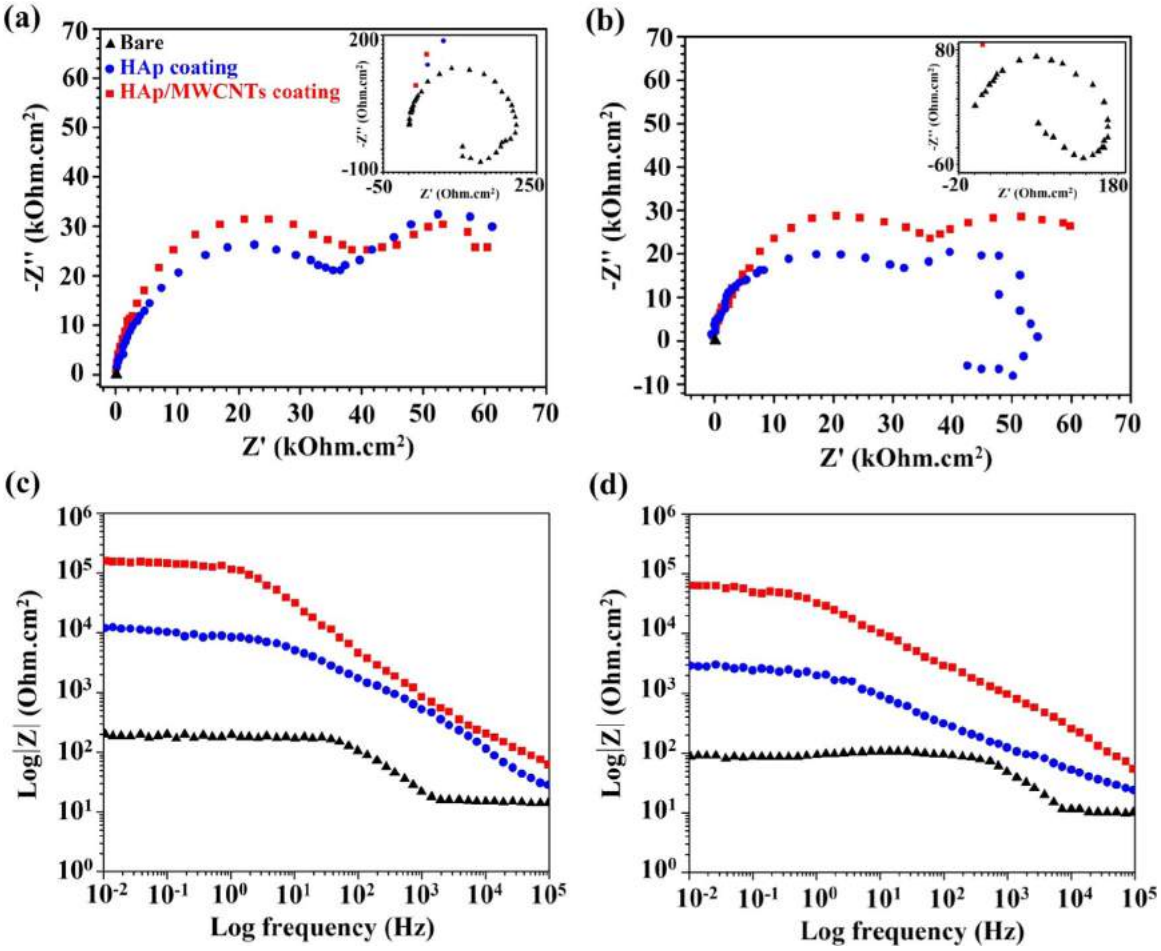

Fig. 6. Nyquist and Bode modulus plots of different samples after (left) 60 min and (right) after 30 h of immersion in SBF.

impedance modulus clearly reveal that the corrosion resistance is decreased after 30 h of immersion.

Both HAp and HAp/MWCNTs coated samples show two time constants after 60 min of immersion (Fig. 6a). The first one in the high frequencies relating to the coating and the other one in the low frequencies corresponding to the polarization resistance at the substrate surface beneath the coating. Although both coatings reveal similar behaviors after 60 min, due to the bigger capacitance loop and impedance modulus, the corrosion resistance of the HAp/MWCNTs coating is higher than the HAp one. This can be firstly attributed to the more adhesion between HAp splats due to MWCNTs bridging, and consequently, diffusion of corrosive species becomes more difficult. In addition, the presence of lower amounts of secondary phases in the HAp/MWCNTs coating improves its corrosion resistance [9,35]. Although this behavior is nearly maintained for the HAp/MWCNTs coating even after 30 h of immersion, HAp coating suffers from considerable corrosion after this exposure time. As can be seen from Fig. 6b, a new time constant (inductive loop) at low frequency ranges appears in the Nyquist plot of HAp coating which in turn indicating the occurrence of localized corrosion beneath the coating. Thus, these results demonstrate that the HAp/MWCNTs composite coating can effectively protect the Mg alloy from corrosion.

In order to quantitatively analyze the EIS data, experimental results were fitted to the electrical equivalent circuits shown in Fig. 7. These circuits reveal the electrolyte resistance, R_s, constant phase element of the double layer, CPE_{dl}, polarization resistance, R_p, resistance and inductance of the species adsorbed on the substrate surface, R_l and L_l, constant phase element of coating, CPE_c and coating pores resistance, R_c. The constant phase elements consist of P and n which are the admittance of the CPE and the deviation parameter, respectively [31]. From the fitting data listed in Table 5, it can be found that HAp/MWCNTs coating always shows higher R_p and lower C_{dl} values (especially after 30 h of immersion) which confirm that this coating exhibits a better and more stable corrosion performance than other samples.

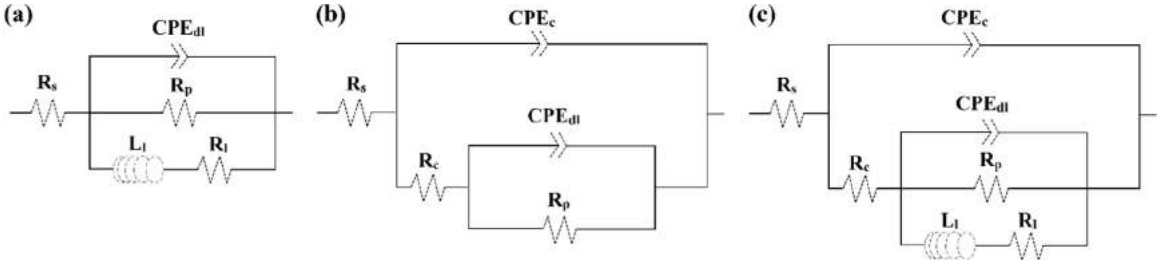

Fig. 7. Equivalent circuits used to fit the EIS data for (a) uncoated alloy, (b) HAp (only after 60 min of immersion) and HAp/MWCNTs coatings and (c) HAp (only after 30 h of immersion).

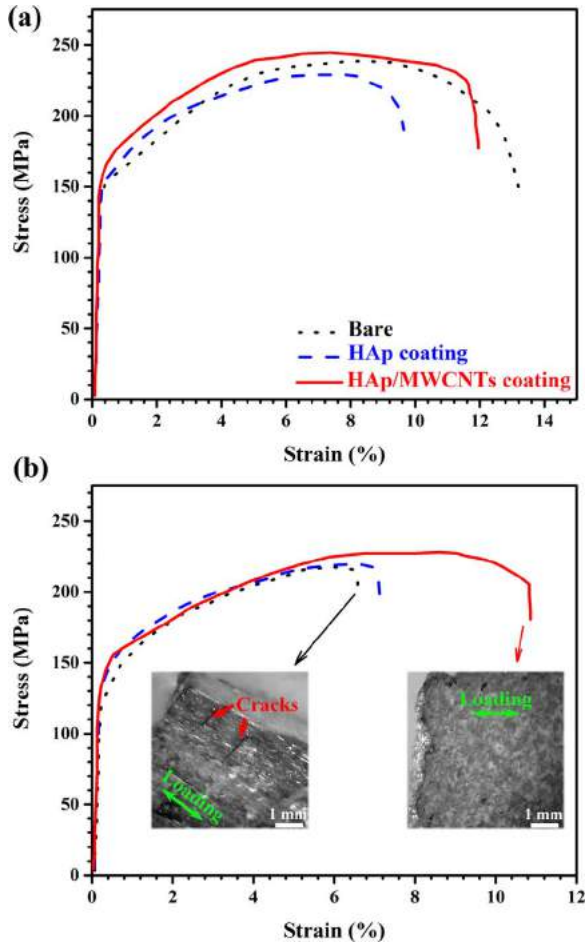

Fig. 8. Slow-strain curves of the SSRT tests for different samples in (a) air and (b) SBF. The surface appearance of bare and HAp/MWCNTs coated samples after SSRT test in the SBF has been shown as the inset.

Table 4
The electrochemical parameters extracted from the polarization curves.

Sample	E_{corr} (V vs. SCE)	i_{corr} (A/cm^2)	β_a (mV/decade)	$-\beta_c$ (mV/decade)
Bare	−1.521	3.5×10^{-4}	167	125
HAp coating	−1.465	4.1×10^{-6}	142	169
HAp/MWCNTs coating	−1.417	3.7×10^{-7}	157	171

3.3. SCC susceptibility and signal interpretation

The stress–strain curves of different samples tested in air and SBF are shown in Fig. 8. Mechanical properties data are also presented in Table 6. The SCC susceptibility of the samples was evaluated according to elongation percentage loss (ε_{loss}) in SBF media and calculated by Eq. (3) [36]:

$$\varepsilon_{loss} = \left(1 - \left(\frac{\varepsilon_{air}}{\varepsilon_{SBF}}\right)\right) \times 100 \quad (3)$$

Where ε_{air} and ε_{SBF} are the elongation percentages measured after SSRT in air and SBF media, respectively. As can be found from Table 6, uncoated AZ31 Mg alloy possesses the highest ε_{loss} (52.9%) i.e. this alloy is extremely susceptible to SCC. Comparable results have been reported by other researchers [36]. On the other hand, in the presence of HAp coating or HAp/MWCNTs one, the SCC susceptibility is significantly decreased so that the ε_{loss} of these coatings is 26.8% and 9.8%, respectively. Since the twinning deformation is the source of SCC susceptibility [37], it is necessary to perform a detailed fractography on the fracture surfaces of samples. Typical fracture surfaces of different samples after SSRT in SBF are shown in Fig. 9. It can be seen from Fig. 9a that the fracture surface of the uncoated AZ31 Mg mainly consists of the cleavage facets. On the other hand, in the presence of HAp or HAp/MWCNTs coating, the fracture behavior is altered (Figs. 9b and c). The fracture surfaces of coated samples have been composed of cleavage facets and dimple-like (especially at the edge of facets) morphologies so that the fraction of dimple-like areas has been obviously increased in the case of HAp/MWCNTs coated one. In fact, in the presence of MWCNTs, the fracture surface goes toward a semi-ductile fracture surface (mixed mode: ductile and brittle). These experimental data show that the fracture mechanism of AZ31 Mg alloy can be affected and improved in the presence of plasma sprayed coatings. Meanwhile, this improvement is more remarkable for HAp/MWCNTs coated sample. In line with what we expressed to interpret the fracture toughness, it can be claimed that the MWCNTs can act as bridges between HAp splats and restrict the opening of the cracks. So, the crack propagating through HAp splats gets restricted when it comes in the vicinity of MWCNTs and more energy is required for debonding. Other researchers also studied the MWCNTs bridging phenomenon and its effects on the toughening of HAp/MWCNTs composite structures [30,38].

As shown in Fig. 10, the electrochemical noise (EN) of samples during SSRT test was also measured. A relatively monotonic increase in current and a nearly steady decrease in voltage without certain transients are observed in Fig. 10. Based on these variations, it can be stated that the degradation process (including the formation of loose monolayers and their rupturing [39]) is continuously occurred in different samples. In addition, it is implied that the degradation mechanism of different samples is almost similar and their difference is summarized in different kinetics for degradation reactions. As it is clear (Fig. 10), HAp/MWCNTs coated sample has the highest failure time. This matter can be also confirmed by power spectral density (PSD) plots. For this purpose, EN data were analyzed in the frequency domain. The power spectral densities of current (PSD_i) were calculated as follows [39] (Fig. 11):

$$\log PSD_i = A_i + S_i \log f\,(i^2 Hz^{-1}) \quad (7)$$

Where A_i and S_i are respectively the noise intensity and the roll-off slope of PSD_i plot. The A_i and S_i parameters can reveal some information about the relative corrosion resistance and kind of corrosion (general and/or localized corrosion), respectively [40]. Since the PSD_i plot of HAp/MWCNTs coated sample appears lower than other samples, it may be found that its corrosion resistance is higher than other samples. In addition, the S_i values of the bare sample, HAp coated and HAp/MWCNTs one are respectively –1.65, –1.59 and –1.61 implying that for all samples a continuous degradation process is occurring on the surface [38,39]. Similar to electrochemical corrosion results, in the presence of SSRT loading, it can be also claimed that the MWCNTs-bridging and higher adhesion between the HAp splats can efficiently retard and/or prevent the diffusion of corrosive species and postpone the fracture time (see fracture times in Fig. 10).

4. Conclusions

1. The uniform HAp/MWCNTs coating with a thickness of 125.6 ± 9.1 μm was produced on the surface of AZ31 Mg alloy by plasma spray technique. This coating was mainly composed of HAp, CaO, and dicalcium phosphate dihydrate phases.
2. Due to the high melting point of MWCNTs, they remain intact during plasma spraying and act as bridges between the melted/semi-melted splats. In this way, they increase the fracture toughness of HAp coating from 0.91 ± 0.16 MPa/m$^{0.5}$ to 2.13 ± 0.29 MPa/m$^{0.5}$.

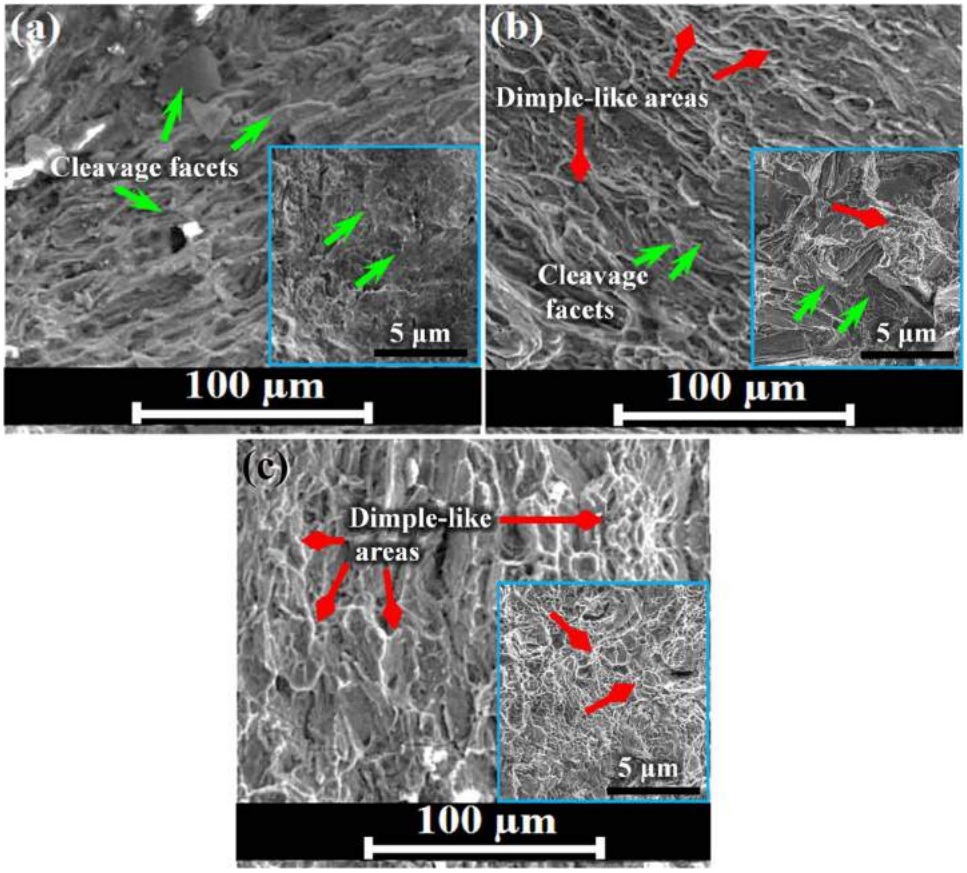

Fig. 9. The fracture surface of different samples: (a) bare AZ31 Mg alloy, (b) HAp coated, and (c) HAp/MWCNs coated samples.

3. HAp/MWCNTs coating shifts the corrosion potential toward noble values; E_{corr} of the AZ31 Mg alloy increased from −1.521 V vs. SCE to –1.465 and −1.417 V vs. SCE for HAp and HAp/MWCNTs coatings, respectively. In addition, corrosion current density of HAp/MWCNTs coated sample (3.7×10^{-7} A/cm^2) is respectively one order of magnitude (4.1×10^{-6} A/cm^2) and three orders of magnitude (3.5×10^{-4} A/cm^2) lower than HAp coated sample and bare one.
4. HAp/MWCNTs coating can efficiently decrease the SCC susceptibility of AZ31 Mg alloy. Fractured surfaces showed that in the presence of this coating the fracture mode is altered from cleavage mode to a dimple-like one.
5. The combination of SEM imaging, mechanical properties, EIS and EN measurements revealed that in the presence or absence of SSRT loading, HAp coating reinforced by MWCNTs shows higher resistance against crack formation: so, it can effectively prevent or retard the penetration of aggressive chloride ions or water molecules. Hence, HAp/MWCNTs coated sample possesses a good corrosion resistance.

Table 6
The results of the SSRT tests on different samples in air and SBF.

Sample	UTS (MPa)	YS (MPa)	Elongation (%)
In air			
Bare	239	139	13.27
HAp coating	229	146	9.65
HAp/MWCNTs coating	247	152	11.94
In SBF			
Bare	217	119	6.25
HAp coating	222	123	7.06
HAp/MWCNTs coating	231	139	10.77

Acknowledgements

The authors thank Mr. Hashem Teimourinejad, Dr. Masood Naddafian, Mr. Afshin Nazarnejatizadeh, Mr. Omid Sadeghi and Mr. Javad Pouryahya (Park-e Mashahir Group) for the valuable consultation.

Table 5
The electrochemical data obtained after fitting the EIS data to the equivalent circuits shown in Fig. 7.

Sample	R_s (Ω cm^2)	R_p (Ω cm^2)	CPE_{dl}		L_l (H/cm^2)	R_l (Ω cm^2)	R_c (Ω cm^2)	CPE_c	
			P (μF/cm^2)	n				P (μF/cm^2)	n
After 60 min immersion									
Bare	21.6	246.1	2.1×10^{-5}	0.95	187.2	216.5	–	–	–
Hap coating	111.3	3.3×10^{5}	7.3×10^{-8}	0.85	–	–	1.2×10^{5}	2.6×10^{-7}	0.61
HAp/MWCNT coating	107.8	3.7×10^{5}	1.4×10^{-8}	0.84	–	–	1.8×10^{5}	1.1×10^{-7}	0.68
After 30 h immersion									
Bare	8.2	105.9	3.7×10^{-4}	0.81	152.7	143.5	–	–	–
Hap coating	92.5	9.2×10^{4}	2.8×10^{-7}	0.56	717.4	8.8×10^{4}	4.2×10^{3}	1.5×10^{-5}	0.50
HAp/MWCNT coating	99.1	2.4×10^{5}	8.5×10^{-7}	0.63	–	–	9.3×10^{4}	8.2×10^{-6}	0.57

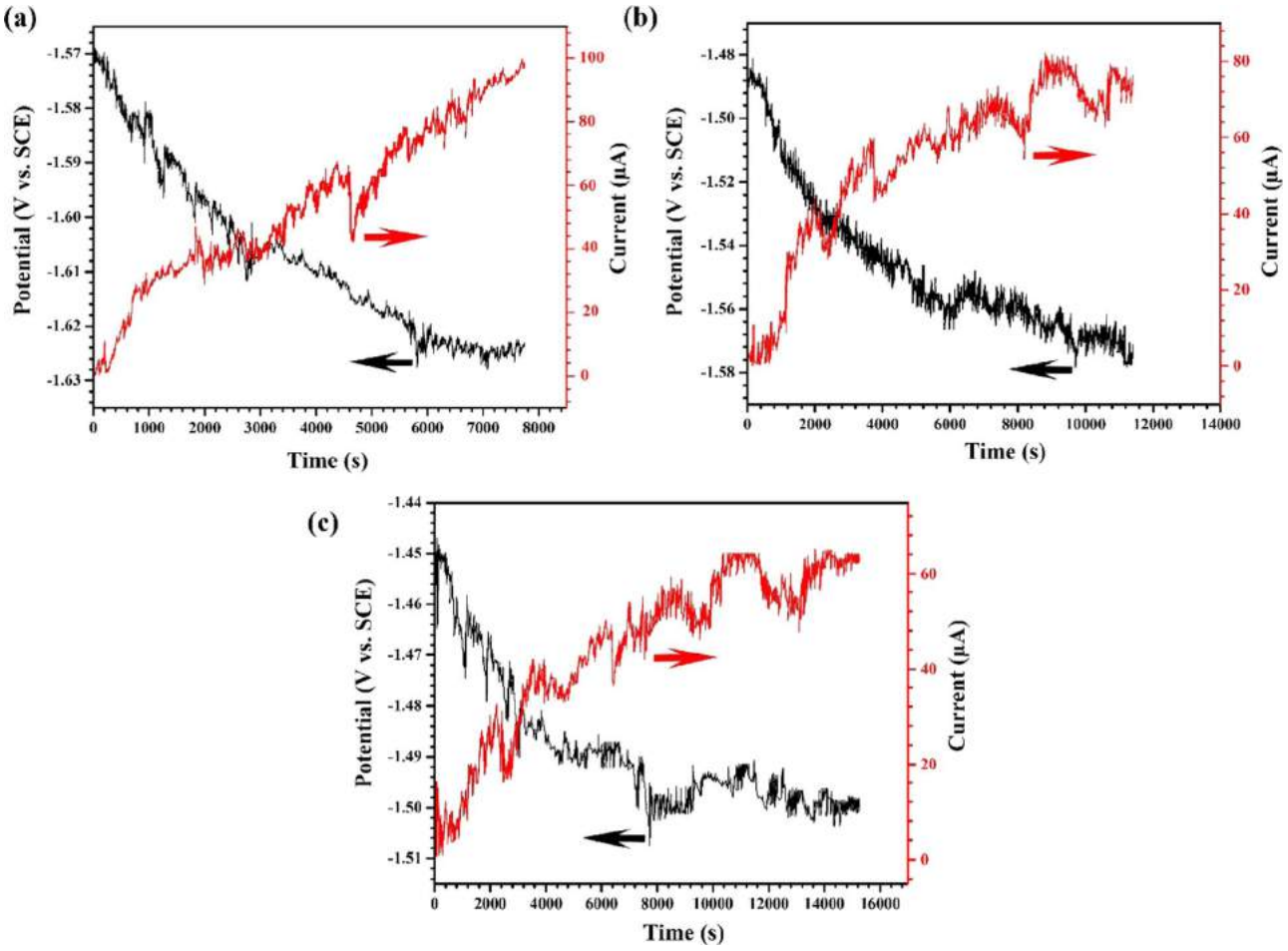

Fig. 10. Potential and current changes with the time during SSRT.

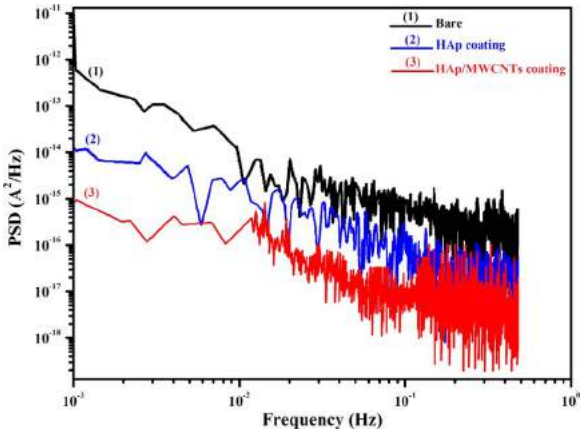

Fig. 11. The PSD_i of different samples during SSRT.

References

[1] X. Li, C. Chu, P.K. Chu, Effects of external stress on biodegradable orthopedic materials: a review, Bioact. Mater. 1 (2016) 77–84.

[2] N. Li, Y. Zheng, Novel magnesium alloys developed for biomedical application: a review, J. Mater. Sci. Technol. 29 (2013) 489–502.

[3] S. Mehdi Mirhadi, A. Abbas Nourbakhsh, N. Lotfian, B. Hosseini, Strength development, bioactivity and biodegradability of forsterite nanostructure scaffold, Ceram. Int. 41 (2015) 1361–1365, http://dx.doi.org/10.1016/j.ceramint.2014.09.069.

[4] S. Tabasum, A. Noreen, A. Kanwal, M. Zuber, M.N. Anjum, K.M. Zia, Glycoproteins functionalized natural and synthetic polymers for prospective biomedical applications: a review, Int. J. Biol. Macromol. (2017).

[5] F. Heidari, M. Razavi, M.E. Bahrololoom, M. Yazdimamaghani, M. Tahriri, H. Kotturi, L. Tayebi, Evaluation of the mechanical properties, in vitro biodegradability and cytocompatibility of natural chitosan/hydroxyapatite/nano-Fe3O4 composite, Ceram. Int. 44 (2018) 275–281, http://dx.doi.org/10.1016/j.ceramint.2017.09.170.

[6] M. Jamesh, S. Kumar, T.S.N.S. Narayanan, Electrodeposition of hydroxyapatite coating on magnesium for biomedical applications, J. Coat. Technol. Res. 9 (2012) 495–502.

[7] H.B. Jiang, G. Wu, S.-B. Lee, K.-M. Kim, Achieving controllable degradation of a biomedical magnesium alloy by anodizing in molten ammonium bifluoride, Surf. Coat. Technol. 313 (2017) 282–287.

[8] D. Hong, D.-T. Chou, O.I. Velikokhatnyi, A. Roy, B. Lee, I. Swink, I. Issaev, H.A. Kuhn, P.N. Kumta, Binder-jetting 3D printing and alloy development of new biodegradable Fe-Mn-Ca/Mg alloys, Acta Biomater. 45 (2016) 375–386.

[9] T.M. Mukhametkaliyev, M.A. Surmeneva, A. Vladescu, C.M. Cotrut, M. Braic, M. Dinu, M.D. Vranceanu, I. Pana, M. Mueller, R.A. Surmenev, A biodegradable AZ91 magnesium alloy coated with a thin nanostructured hydroxyapatite for improving the corrosion resistance, Mater. Sci. Eng. C 75 (2017) 95–103.

[10] H. Yang, K. Xia, T. Wang, J. Niu, Y. Song, Z. Xiong, K. Zheng, S. Wei, W. Lu, Growth, in vitro biodegradation and cytocompatibility properties of nano-hydroxyapatite coatings on biodegradable magnesium alloys, J. Alloy. Compd. 672 (2016) 366–373.

[11] M.P. Staiger, A.M. Pietak, J. Huadmai, G. Dias, Magnesium and its alloys as orthopedic biomaterials: a review, Biomaterials 27 (2006) 1728–1734.

[12] J. Ma, M. Thompson, N. Zhao, D. Zhu, Similarities and differences in coatings for magnesium-based stents and orthopaedic implants, J. Orthop. Transl. 2 (2014) 118–130.

[13] N.T. Kirkland, N. Birbilis, M.P. Staiger, Assessing the corrosion of biodegradable magnesium implants: a critical review of current methodologies and their limitations, Acta Biomater. 8 (2012) 925–936.

[14] N.-E.L. Saris, E. Mervaala, H. Karppanen, J.A. Khawaja, A. Lewenstam, Magnesium: an update on physiological, clinical and analytical aspects, Clin. Chim. Acta 294 (2000) 1–26.

[15] M.I. Jamesh, G. Wu, Y. Zhao, D.R. McKenzie, M.M.M. Bilek, P.K. Chu, Electrochemical corrosion behavior of biodegradable Mg–Y–RE and Mg–Zn–Zr alloys in Ringer's solution and simulated body fluid, Corros. Sci. 91 (2015) 160–184.

[16] X. Lin, X. Wang, L. Tan, P. Wan, X. Yu, Q. Li, K. Yang, Effect of preparation parameters on the properties of hydroxyapatite containing micro-arc oxidation coating on biodegradable ZK60 magnesium alloy, Ceram. Int. 40 (2014) 10043–10051,

http://dx.doi.org/10.1016/j.ceramint.2014.02.104.
[17] H.R. Bakhsheshi-Rad, E. Hamzah, A.F. Ismail, M. Kasiri-Asgarani, M. Daroonparvar, S. Parham, N. Iqbal, M. Medraj, Novel bi-layered nanostructured SiO_2/Ag-FHAp coating on biodegradable magnesium alloy for biomedical applications, Ceram. Int. 42 (2016) 11941–11950, http://dx.doi.org/10.1016/j.ceramint.2016.04.119.
[18] J. Li, X. He, R. Hang, X. Huang, X. Zhang, B. Tang, Fabrication and corrosion behavior of TiO_2 nanotubes on AZ91D magnesium alloy, Ceram. Int. 43 (2017) 13683–13688, http://dx.doi.org/10.1016/j.ceramint.2017.07.079.
[19] S.R. Kiahosseini, A. Afshar, M. Mojtahedzadeh Larijani, M. Yousefpour, Structural and corrosion characterization of hydroxyapatite/zirconium nitride-coated AZ91 magnesium alloy by ion beam sputtering, Appl. Surf. Sci. 401 (2017) 172–180, http://dx.doi.org/10.1016/j.apsusc.2017.01.022.
[20] N. Yu, S. Cai, F. Wang, F. Zhang, R. Ling, Y. Li, Y. Jiang, G. Xu, Microwave assisted deposition of strontium doped hydroxyapatite coating on AZ31 magnesium alloy with enhanced mineralization ability and corrosion resistance, Ceram. Int. 43 (2017) 2495–2503, http://dx.doi.org/10.1016/j.ceramint.2016.11.050.
[21] S. Shen, S. Cai, Y. Li, R. Ling, F. Zhang, G. Xu, F. Wang, Microwave aqueous synthesis of hydroxyapatite bilayer coating on magnesium alloy for orthopedic application, Chem. Eng. J. 309 (2017) 278–287, http://dx.doi.org/10.1016/j.cej.2016.10.043.
[22] K. Balani, R. Anderson, T. Laha, M. Andara, J. Tercero, E. Crumpler, A. Agarwal, Plasma-sprayed carbon nanotube reinforced hydroxyapatite coatings and their interaction with human osteoblasts in vitro, Biomaterials 28 (2007) 618–624, http://dx.doi.org/10.1016/j.biomaterials.2006.09.013.
[23] Y. Chen, Y.Q. Zhang, T.H. Zhang, C.H. Gan, C.Y. Zheng, G. Yu, Carbon nanotube reinforced hydroxyapatite composite coatings produced through laser surface alloying, Carbon 44 (2006) 37–45, http://dx.doi.org/10.1016/j.carbon.2005.07.011.
[24] K. Balani, Y. Chen, S.P. Harimkar, N.B. Dahotre, A. Agarwal, Tribological behavior of plasma-sprayed carbon nanotube-reinforced hydroxyapatite coating in physiological solution, Acta Biomater. 3 (2007) 944–951, http://dx.doi.org/10.1016/j.actbio.2007.06.001.
[25] A.A. White, S.M. Best, I.A. Kinloch, Hydroxyapatite–carbon nanotube composites for biomedical applications: a review, Int. J. Appl. Ceram. Technol. 4 (2007) 1–13.
[26] L. Choudhary, R.K. Singh Raman, Magnesium alloys as body implants: fracture mechanism under dynamic and static loadings in a physiological environment, Acta Biomater. 8 (2012) 916–923, http://dx.doi.org/10.1016/j.actbio.2011.10.031.
[27] X. Pei, J. Wang, Q. Wan, L. Kang, M. Xiao, H. Bao, Functionally graded carbon nanotubes/hydroxyapatite composite coating by laser cladding, Surf. Coat. Technol. 205 (2011) 4380–4387, http://dx.doi.org/10.1016/j.surfcoat.2011.03.036.
[28] T. Akasaka, F. Watari, Y. Sato, K. Tohji, Apatite formation on carbon nanotubes, Mater. Sci. Eng. C 26 (2006) 675–678, http://dx.doi.org/10.1016/j.msec. 2005.03.009.
[29] L.-G. Yu, K.A. Khor, H. Li, P. Cheang, Effect of spark plasma sintering on the microstructure and in vitro behavior of plasma sprayed HA coatings, Biomaterials 24 (2003) 2695–2705, http://dx.doi.org/10.1016/S0142-9612(03)00082-6.
[30] D. Lahiri, S. Ghosh, A. Agarwal, Carbon nanotube reinforced hydroxyapatite composite for orthopedic application: a review, Mater. Sci. Eng. C 32 (2012) 1727–1758, http://dx.doi.org/10.1016/j.msec. 2012.05.010.
[31] S. Pour-Ali, A. Kiani-Rashid, A. Babakhani, A. Davoodi, Enhanced protective properties of epoxy/polyaniline-camphorsulfonate nanocomposite coating on an ultrafine-grained metallic surface, Appl. Surf. Sci. 376 (2016) 121–132, http://dx.doi.org/10.1016/j.apsusc.2016.03.131.
[32] T.S. Lim, H.S. Ryu, S.-H. Hong, Electrochemical corrosion properties of CeO2-containing coatings on AZ31 magnesium alloys prepared by plasma electrolytic oxidation, Corros. Sci. 62 (2012) 104–111, http://dx.doi.org/10.1016/j.corsci.2012.04.043.
[33] L.-Y. Cui, S.-D. Gao, P.-P. Li, R.-C. Zeng, F. Zhang, S.-Q. Li, E.-H. Han, Corrosion resistance of a self-healing micro-arc oxidation/polymethyltrimethoxysilane composite coating on magnesium alloy AZ31, Corros. Sci. 118 (2017) 84–95, http://dx.doi.org/10.1016/j.corsci.2017.01.025.
[34] S. Pour-Ali, A. Kiani-Rashid, A. Babakhani, A. Davoodi, Enhanced protective properties of epoxy/polyaniline-camphorsulfonate nanocomposite coating on an ultrafine-grained metallic surface, Appl. Surf. Sci. 376 (2016) 121–132, http://dx.doi.org/10.1016/j.apsusc.2016.03.131.
[35] S. Pour-Ali, A. Kiani-Rashid, A. Babakhani, Improved corrosion inhibition of 3-amino-1, 2, 4-triazole on mild steel electrode in HCl solution using surface nanocrystallization, Int. J. Mater. Res. 107 (2016) 1031–1040.
[36] L.C. Tsao, Stress-corrosion cracking susceptibility of AZ31 alloy after varied heat-treatment in 3.5 wt% NaCl solution, Int. J. Mater. Res. 101 (2010) 1166–1171.
[37] M. Bobby Kannan, W. Dietzel, C. Blawert, A. Atrens, P. Lyon, Stress corrosion cracking of rare-earth containing magnesium alloys ZE41, QE22 and Elektron 21 (EV31A) compared with AZ80, Mater. Sci. Eng. A 480 (2008) 529–539, http://dx.doi.org/10.1016/j.msea.2007.07.070.
[38] S. Kalmodia, S. Goenka, T. Laha, D. Lahiri, B. Basu, K. Balani, Microstructure, mechanical properties, and in vitro biocompatibility of spark plasma sintered hydroxyapatite–aluminum oxide–carbon nanotube composite, Mater. Sci. Eng. C 30 (2010) 1162–1169, http://dx.doi.org/10.1016/j.msec. 2010.06.009.
[39] T. Zhang, Y. Shao, G. Meng, F. Wang, Electrochemical noise analysis of the corrosion of AZ91D magnesium alloy in alkaline chloride solution, Electrochim. Acta 53 (2007) 561–568, http://dx.doi.org/10.1016/j.electacta.2007.07.014.
[40] R.G. Kelly, J.R. Scully, D. Shoesmith, R.G. Buchheit, Electrochemical Techniques in Corrosion Science and Engineering, CRC Press, 2002.